

UNCLASSIFIED

Defense Technical Information Center
Compilation Part Notice

ADP013621

TITLE: High-Order Schemes for DNS/LES and CAA on Curvilinear
Dynamic Meshes

DISTRIBUTION: Approved for public release, distribution unlimited

This paper is part of the following report:

TITLE: DNS/LES Progress and Challenges. Proceedings of the Third
AFOSR International Conference on DNS/LES

To order the complete compilation report, use: ADA412801

The component part is provided here to allow users access to individually authored sections of proceedings, annals, symposia, etc. However, the component should be considered within the context of the overall compilation report and not as a stand-alone technical report.

The following component part numbers comprise the compilation report:

ADP013620 thru ADP013707

UNCLASSIFIED

HIGH-ORDER SCHEMES FOR DNS/LES AND CAA ON CURVILINEAR DYNAMIC MESHES

M. VISBAL, D. GAITONDE AND D. RIZZETTA

Air Force Research Laboratory

Wright-Patterson Air Force Base, Ohio 45433-7521

1. Introduction

Despite significant progress in computational sciences, challenges persist in the accurate numerical simulation of a broad spectrum of dynamic, multi-physics phenomena relevant to aerospace systems. These challenging areas include the direct and large-eddy simulation of turbulence, aeroacoustics, fluid/structure interactions, electromagnetics, and magneto-gasdynamics. In order to reduce the severe computational requirements of standard low-order schemes, higher-order formulations, as well as massively parallel approaches are being actively pursued. Due to their spectral-like resolution and ease of extension to multiple disciplines, high-order compact schemes[1] represent an attractive choice for reducing dispersion, anisotropy and dissipation errors associated with spatial discretizations. Until recently, these schemes have mostly been used in conjunction with explicit time-integration methods to address complex flow physics on simple Cartesian geometries.

Recent work performed at the Air Force Research Laboratory [2, 3, 4, 5, 6, 7] has extended the use of compact algorithms to more practical applications. This has been achieved through the development and improved treatment of the various critical elements comprising the overall numerical approach. Particular attention has been focused on enhanced high-order (up to 10th-order) low-pass filtering techniques, accurate and robust near-boundary formulations, proper metric evaluation, multi-domain implementation strategies, and sub-iterative implicit time-advancement methods. As an outcome of this sustained effort, the highly accurate compact algorithm has been successfully applied to efficiently solve a range of multi-physics phenomena described by the Euler, Navier-Stokes and MHD equations on 3-D curvilinear and dynamic grids using either explicit or implicit time integration approaches.

These high-fidelity computational tools are currently being transitioned to the multidisciplinary simulation of complex phenomena relevant to Air Force systems, including: weapon-bay cavity acoustics, hypersonic flow control, high- angle-of-attack aerodynamics, and non-linear aeroelastic response. A brief description of the governing equations, the various elements of the numerical approach, as well as a few representative applications are included in this paper.

2. Governing Equations

In order to develop a procedure suitable for nonlinear fluid dynamic, aeroacoustic and aeroelastic applications over complex configurations, the full Navier-Stokes equations are selected and are cast in strong conservative form introducing a general time-dependent curvilinear coordinate transformation $(x, y, z, t) \rightarrow (\xi, \eta, \zeta, \tau)$. In vector notation, and employing non-dimensional variables, these equations are:

$$\frac{\partial}{\partial \tau} \left(\frac{\vec{U}}{J} \right) + \frac{\partial \hat{F}}{\partial \xi} + \frac{\partial \hat{G}}{\partial \eta} + \frac{\partial \hat{H}}{\partial \zeta} = \frac{1}{Re} \left[\frac{\partial \hat{F}_v}{\partial \xi} + \frac{\partial \hat{G}_v}{\partial \eta} + \frac{\partial \hat{H}_v}{\partial \zeta} \right] + \vec{S}/J \quad (1)$$

where $\vec{U} = \{\rho, \rho u, \rho v, \rho w, \rho E\}$ denotes the solution vector, $\hat{F}, \hat{G}, \hat{H}, \hat{F}_v, \hat{G}_v, \hat{H}_v$ are the fluxes, S denotes a source term, and $J = \partial(\xi, \eta, \zeta, \tau) / \partial(x, y, z, t)$ is the transformation Jacobian which for dynamic meshes is a function of time.

3. Numerical Method

3.1. SPATIAL DISCRETIZATION

A finite-difference approach is employed to discretize the governing equations. This choice is motivated by the relative ease of formal extension to higher-order accuracy. For any scalar quantity, ϕ , such as a metric, flux component or flow variable, the spatial derivative ϕ' is obtained in the transformed plane by solving the tridiagonal system:

$$\Gamma \phi'_{i-1} + \phi'_i + \Gamma \phi'_{i+1} = b \frac{\phi_{i+2} - \phi_{i-2}}{4} + a \frac{\phi_{i+1} - \phi_{i-1}}{2} \quad (2)$$

where Γ , a and b determine the spatial properties of the algorithm. The formula yields the compact five-point, sixth-order $C6$, and three-point fourth-order $C4$ schemes [1] with $\Gamma = 1/3$, $a = 14/9$, $b = 1/9$ and $\Gamma = 1/4$, $a = 3/2$, $b = 0$ respectively. Equation (2) also incorporates the standard explicit fourth-order ($E4$) and second-order ($E2$) approaches for which the coefficients are $(\Gamma = 0, a = 4/3, b = -1/3)$ and $(\Gamma = 0, a = 1, b = 0)$ respectively. The dispersion characteristics and truncation error of the above

schemes can be found in Refs. [1, 5]. It should be noted that for a given order of accuracy, the compact schemes are significantly superior to their explicit (non-compact) counterparts. The scheme of Eqn. (2) cannot be applied at a few points near each boundary where the stencil protrudes the domain. Here, special one-sided boundary schemes, such as those described in Refs. [5, 8] are employed.

In order to compute the residual, the derivatives of the inviscid fluxes are obtained by first forming the fluxes at the nodes and subsequently differentiating each component with the above formulas. Viscous terms are obtained by first computing derivatives of the primitive variables. The components of the viscous flux are then constructed at each node and differentiated by a second application of the same scheme. Although this approach is not as accurate as that in which a Pade-type scheme is employed directly for the second-derivative, it is significantly cheaper to implement in curvilinear coordinates. As previously demonstrated in Ref. [2], successive differentiation yields an accurate and stable method in conjunction with the added filtering component which is described next.

3.2. HIGH-ORDER FILTERING SCHEME

Compact-difference discretizations, like other centered schemes, are non-dissipative and are therefore susceptible to numerical instabilities due to the unrestricted growth of high-frequency modes. These difficulties originate from several sources including mesh non-uniformity, approximate boundary conditions and nonlinear flow features. In order to extend the present solver to practical simulations, while retaining the improved accuracy of the spatial compact discretization, a high-order implicit filtering technique [2, 4] is incorporated. If a typical component of the solution vector is denoted by ϕ , filtered values $\hat{\phi}$ satisfy,

$$\alpha_f \hat{\phi}_{i-1} + \hat{\phi}_i + \alpha_f \hat{\phi}_{i+1} = \sum_{n=0}^N \frac{a_n}{2} (\phi_{i+n} + \phi_{i-n}) \quad (3)$$

Equation (3), with the proper choice of coefficients, provides an $2N$ th-order formula on a $2N + 1$ point stencil. The $N + 1$ coefficients, a_0, a_1, \dots, a_N , are derived in terms of α_f with Taylor- and Fourier-series analyses and are found in Refs. [2, 3] along with some spectral filter responses. The adjustable parameter α_f satisfies the inequality $-0.5 < \alpha_f < 0.5$, with higher values of α_f corresponding to a less dissipative filter. In multi-dimensional problems the filter operator is applied sequentially in each coordinate direction. For the near-boundary points, the filtering strategies described in Refs. [2, 3] are employed. Up to tenth-order filter formulas have been successfully applied to solve the Maxwell [4], Navier-Stokes [2, 9, 10, 11], and MHD [12] equations in curvilinear geometries.

3.3. METRIC EVALUATION FOR CURVILINEAR DYNAMIC MESHES

The extension of high-order schemes to 3-D curvilinear meshes demands that issues of freestream preservation and metric cancellation be carefully addressed. These errors, which arise in finite-difference discretizations of governing equations written in strong-conservation form, can catastrophically degrade the fidelity of standard second-order as well as higher-order approaches [3]. In deriving the flow equations in strong-conservation form, the following metric identities have been implicitly invoked,

$$I_1 = (\xi_x/J)_\xi + (\eta_x/J)_\eta + (\zeta_x/J)_\zeta = 0 \quad (4)$$

$$I_2 = (\xi_y/J)_\xi + (\eta_y/J)_\eta + (\zeta_y/J)_\zeta = 0 \quad (5)$$

$$I_3 = (\xi_z/J)_\xi + (\eta_z/J)_\eta + (\zeta_z/J)_\zeta = 0 \quad (6)$$

$$I_4 = (1/J)_\tau + (\xi_t/J)_\xi + (\eta_t/J)_\eta + (\zeta_t/J)_\zeta = 0 \quad (7)$$

In Ref. [2] it was shown that on stretched curvilinear 2-D meshes, the compact scheme exhibits freestream preservation when the metrics are evaluated with the same finite-difference expressions as those employed for the fluxes. It was also demonstrated that the practice of prescribing *analytic* metrics on stretched curvilinear grids can lead to unacceptable errors and therefore should in general be avoided. The previous straightforward approach of calculating the metrics, although effective in 2-D, fails to provide metric cancellation for general 3-D curvilinear configurations. To illustrate this point, consider the standard metric relations:

$$\begin{aligned} \xi_x/J &= y_\eta z_\zeta - y_\zeta z_\eta \\ \eta_x/J &= y_\zeta z_\xi - y_\xi z_\zeta \\ \zeta_x/J &= y_\xi z_\eta - y_\eta z_\xi \end{aligned} \quad (8)$$

associated with the identity I_1 . Evaluation of the y and z derivatives in the previous expressions using explicit or compact centered schemes does not satisfy I_1 , and as a result, significant grid-induced errors may appear. To extend the high-order compact scheme to general geometries, the metric terms are rewritten prior to discretization in the equivalent ('conservative') form [13]:

$$\begin{aligned} \xi_x/J &= (y_\eta z)_\zeta - (y_\zeta z)_\eta \\ \eta_x/J &= (y_\zeta z)_\xi - (y_\xi z)_\zeta \\ \zeta_x/J &= (y_\xi z)_\eta - (y_\eta z)_\xi \end{aligned} \quad (9)$$

Similar expressions are employed for the remaining metric terms in order to satisfy the identities I_2 and I_3 above. When the transformation metrics are

recast in this manner, and the derivatives are evaluated with the same high-order formulas employed for the fluxes, freestream preservation is again recovered in general time-invariant 3-D curvilinear geometries [3].

For deforming and moving meshes, the identity I_4 must be also satisfied to eliminate metric cancellation errors and to ensure freestream preservation [6]. This metric identity is referred to in the literature [13] as the Geometric Conservation Law (*GCL*). For the time-integration methods employed in this work, the time-derivative term in Eqn. (1) is split using chain-rule differentiation as follows:

$$(\vec{U}/J)_\tau = (1/J)\vec{U}_\tau + \vec{U}(1/J)_\tau \quad (10)$$

Rather than attempting to compute the time derivative of the inverse Jacobian directly from the grid coordinates at various time levels (either analytically or numerically), we simply invoke the *GCL* identity I_4 to evaluate $(1/J)_\tau$, i.e.

$$(1/J)_\tau = -[(\xi_t/J)_\xi + (\eta_t/J)_\eta + (\zeta_t/J)_\zeta] \quad (11)$$

where

$$\begin{aligned} \xi_t/J &= -[x_\tau(\xi_x/J) + y_\tau(\xi_y/J) + z_\tau(\xi_z/J)] \\ \eta_t/J &= -[x_\tau(\eta_x/J) + y_\tau(\eta_y/J) + z_\tau(\eta_z/J)] \\ \zeta_t/J &= -[x_\tau(\zeta_x/J) + y_\tau(\zeta_y/J) + z_\tau(\zeta_z/J)] \end{aligned} \quad (12)$$

For the case of an analytically prescribed dynamic mesh transformation, the grid speeds (x_τ, y_τ, z_τ) are obtained from the corresponding analytic expressions. An example in which the grid speeds are known analytically corresponds to the case of a maneuvering wing when the entire mesh moves in a rigid fashion. In many practical applications involving deforming meshes (e.g. dynamic aeroelastic simulations), the grid speeds are not known a priori, and must therefore be approximated to the desired degree of accuracy employing the evolving grid coordinates at several time levels. As demonstrated in Ref. [6], the high-order method retains its superior accuracy on rapidly distorting meshes when the procedure outlined above is incorporated for the time metrics.

3.4. TIME-INTEGRATION SCHEME

Two different time-integration approaches are incorporated in the present family of solvers. For wave propagation applications, the equations are integrated in time with the classical fourth-order four-stage Runge-Kutta method (*RK4*). The scheme is implemented in low storage form requiring three levels of storage. For wall-bounded viscous flows, the stability constraint of the explicit time-marching scheme is found to render the approach

too restrictive and inefficient. Therefore, the implicit, approximately-factored method of Beam and Warming [14] is also incorporated and augmented through the use of Newton-like subiterations in order to achieve second-order time accuracy. In delta form, the scheme may be written as

$$\begin{aligned}
 & \left[J^{-1p+1} + \phi^i \Delta \tau \delta_\xi^{(2)} \left(\frac{\partial \hat{F}^p}{\partial U} \right) \right] J^{p+1} \times \\
 & \left[J^{-1p+1} + \phi^i \Delta \tau \delta_\eta^{(2)} \left(\frac{\partial \hat{G}^p}{\partial U} \right) \right] J^{p+1} \times \\
 & \left[J^{-1p+1} + \phi^i \Delta \tau \delta_\zeta^{(2)} \left(\frac{\partial \hat{H}^p}{\partial U} \right) \right] \Delta U \\
 & = -\phi^i \Delta \tau \left[J^{-1p+1} \frac{(1+\phi)U^p - (1+2\phi)U^n + \phi U^{n-1}}{\Delta \tau} \right. \\
 & \quad \left. + U^p (1/J)_\tau^p + \delta_\xi \left(\hat{F}^p \right) + \right. \\
 & \quad \left. \delta_\eta \left(\hat{G}^p \right) + \delta_\zeta \left(\hat{H}^p \right) \right]
 \end{aligned} \tag{13}$$

where $\partial \hat{F}/\partial U$ etc are flux Jacobians, δ represents the spatial difference operator and $\Delta U = U^{p+1} - U^p$. For improved efficiency, the method incorporates the diagonalization procedure of Ref. [15]. In addition, nonlinear artificial dissipation terms [16] are appended to the implicit operator to enhance stability. Note that while the derivatives of the flux Jacobians have been obtained to second-order accuracy (denoted with the superscript (2) in Eqn. (13)), those on the right hand side, *i.e.*, in the residual, are evaluated with the compact-difference higher-order method. In order to reduce errors associated with these simplifications, a sub-iteration strategy is employed. Thus, for the first subiteration, $p = 1$, $U^p = U^n$ and as $p \rightarrow \infty$, $U^p \rightarrow U^{n+1}$. Typically, three subiterations are applied per time step. A range of numerical experiments suggests that second-order accuracy in time is adequate for the problems considered [6].

3.5. MULTI-DOMAIN STRATEGY

Domain-decomposition techniques constitute an important component of modern computational strategy. Due to their spatially implicit nature, Pade-type schemes are more difficult to utilize in a multi-domain environment than explicit methods. However, a finite-size overlap can be employed with the present compact/filtering methodology to generate a powerful approach applicable to complicated curvilinear meshes [3]. Figure 1 depicts schematically the problem of a vortex traveling to the right in a rectilinear path. The domain of computation is divided into two parts to be distributed to different processors. Each sub-domain is supplemented with several points from the adjacent sub-domain to form an overlap region, whose details for a five-point vertical overlap are also shown in Fig. 1. Although the overlap points are collocated they have been shown slightly staggered for clarity. Each vertical line is denoted by its i -index. Data is

exchanged between adjacent subdomains at the end of each sub-iteration of the implicit scheme (or each stage of *RK4*), as well as after each application of the filter. The values at points 1 and 2 of Mesh 2 are set to be identically equal to the corresponding updated values at points $IL - 4$ and $IL - 3$ of Mesh 1. Similarly, reciprocal information is transferred through points 4 and 5 of Mesh 2 which “donate” values to points $IL - 1$ and IL of Mesh 1. More details on the accuracy and robustness of the present multi-domain approach can be found in Ref. [3].

4. Results

The previous computational methodology has been successfully demonstrated for a number of applications, including: unsteady vortical flows [2], DNS of pulsed walljet [9] and synthetic jet actuators [17], LES of subsonic and supersonic flows [10, 11], non-linear fluid structure interaction [18], and benchmark problems for acoustic scattering [7] and MHD [12]. In the interest of brevity, only a subset of these results is presented here.

4.1. MULTI-DOMAIN ACOUSTIC SCATTERING SIMULATION

The low dispersion error characteristic of compact-difference schemes is an attractive property in the simulation of wave propagation phenomena associated with acoustic and electromagnetic scattering. In order to demonstrate the capability of the present numerical approach to treat acoustic phenomena in a multiple-domain situation, consider the scattering of a periodic acoustic source with the two-zone overlap configuration shown schematically in Fig. 2a.

The single-domain grid, consisting of 361×321 points, is split along $\theta = 90^\circ$, where extra ξ -lines are added to form a five-point overlap as in Fig. 1. Solutions are advanced separately on each subdomain, and information is exchanged at the overlap points in the manner previously discussed in Section 3.5. The *C6* scheme is employed for interior points along with fourth- and fifth-order compact operators at the boundary and next-to-boundary points respectively whereas *RK4* is utilized for time-integration. In the interior of each domain, a 10th-order filter is utilized while high-order one-sided techniques, described in Refs. [3, 7], are invoked near boundaries. For all filter operators, the coefficient $\alpha_f = 0.45$ is specified.

Figure 2b displays instantaneous pressure contours in the vicinity of the cylinder. It is apparent that the pressure waves cross the grid interface without producing any noticeable disruptions of the interference pattern even though pressure waves generated by the source propagate through the overlap region in an oblique direction to the zonal interface. A quantitative comparison of the single-domain, multiple-domain and analytic solutions

is given in Fig. 2c in terms of the directivity of the radiated sound at $r/D = 5$. The directivity obtained with a 6th-order near-boundary filter in the overlap region is essentially the same as the corresponding single-domain baseline solution, and both results are in excellent agreement with the theoretical solution. These results highlight the potential of the present high-order methodology for domain-decomposition applications on parallel computers. Additional details on the manner in which the high-order filter may be applied to yield a robust farfield radiation treatment for acoustic simulations may be found in Ref. [19].

4.2. DNS OF A PULSED WALLJET

As another example, the method has been employed to simulate the three-dimensional transition of a forced, finite aspect-ratio, plane wall jet [9]. The wall jet configuration considered is shown in Fig. 3a. The main parameters governing the flow are the Reynolds number, the disturbance characteristics at the jet nozzle, the aspect ratio of the channel, and the length of the wall. In the present study, the Reynolds number, based on jet maximum velocity (U_{max}) and nozzle height (h), is 2150. The aspect ratio of the channel is $2b/h = 20$. The mean velocity profile in the normal direction at the nozzle exit is parabolic and corresponds to a fully-developed laminar channel flow in that direction. The flow is forced at the nozzle exit with a frequency of 200Hz and amplitude corresponding to 6% of the jet centerline velocity.

The overall flow structure is shown in Fig. 3b in terms of an iso-surface of vorticity magnitude. The transition process begins with the formation of shear-layer and wall vortex pairs which, due to the energetic forcing, appear close to the nozzle exit and are phased-locked for a short distance downstream. In the process of their spanwise evolution, the rollers are first split into a double-helical structure, which is clearly discernable near the sidewalls. This feature propagates toward the center while also expanding in the radial direction. The spiral vortex branches are wound in a sense opposite to that of the swirl direction of the vortex, but consistent with the direction of the induced axial flow which exists within the vortex core. This vortex branching and helical twisting spreads rapidly through self-induction effects, and eventually reaches the symmetry plane where the vorticity magnitude within the vortex core is drastically diminished (hence the apparent break in the iso-surface, region ' γ ' in Fig. 3b). The ability of the present high-order solver to discern the fine-scale breakdown to turbulence is shown in Fig. 3c which displays contours of vorticity magnitude on a horizontal plane ($y/h = 0.5$). Additional details of the simulation, as well as comparison with high-resolution experimental measurements may be found in Ref. [9].

4.3. LES OF A SPATIALLY-EVOLVING SUPERSONIC BOUNDARY LAYER

This simulation considers a zero-pressure-gradient, flat-plate boundary layer at a Mach number of 2.25 and $Re_\theta \approx 6000$, which corresponds to the computational studies of Refs. [20, 21]. Details of the stretched Cartesian grids and the initial/boundary conditions employed are given in Ref. [11]. In this section, only results (denoted as ‘no-model’) obtained using the 10th-order low-pass filter without the inclusion of an SGS model are considered. Solutions for both the Smagorinsky and dynamic subgrid-scale stress models can be found in Ref. [11].

Figure 4a shows the spanwise-averaged, mean skin-friction coefficient. Downstream of the transition location (which is sensitive to the numerical scheme and forcing employed), the present results compare favorably with those of Ref. [20]. This fact is encouraging since a coarser mesh ($371 \times 61 \times 151$) is used in the present computations with the sixth-order compact approach. The calculations of Ref. [20] were performed on a much finer grid ($971 \times 55 \times 321$) utilizing a fifth-order upwind-bias algorithm for the convective terms. Reasonable agreement in terms of the mean streamwise velocity profile is also shown in Fig. 4b. Finally, contours of the instantaneous spanwise vorticity component at a height of $y^+ \approx 1.0$ are shown in Fig. 4c and display the longitudinal structures characteristic of turbulent wall-bounded flows.

4.4. BOUNDARY-LAYER TRANSITION OVER A FLEXIBLE PANEL

As a final example of a simulation of multi-disciplinary physics with the present methodology, consider a transitional boundary-layer flow over a flexible finite panel embedded in a rigid surface as shown schematically in Fig. 5a. This problem is closely related to classic panel flutter phenomena, as well as to viscous flow over compliant surfaces. The panel of length a and thickness h extends over the region $0.5 \leq x/a \leq 1.5$. The leading-edge region of the plate ($-0.5 \leq x/a \leq 0.0$) is formed by an ellipse of half-thickness $0.05h$ (*i.e.* aspect ratio 10). An additional challenge posed by this aeroelastic simulation is the need to accommodate the surface deflection with a dynamically deforming mesh. The problem has been examined in great detail in Ref. [18] which should be consulted for details regarding boundary condition implementation and mesh resolution studies.

For brevity, only select results obtained at $M_\infty = 0.8$ and $Re_a = 10^5$ are summarized here to highlight the ability of the method to capture the complicated unsteady phenomena under the influence of flow-induced surface deformation. At low values of the dynamic pressure, a steady flow is obtained despite the adverse pressure gradient induced by the downward deflection of the panel. At higher dynamic pressures, however, a travelling-

wave-flutter phenomenon is observed as summarized in Fig. 5b, c. The instantaneous panel shapes (not shown) display a seventh-mode oscillation with a dominant nondimensional frequency $St = fa/U_\infty = 1.52$ which is substantially higher than the fundamental frequency of the elastic plate. The high-mode flexural deflections are observed to travel along the panel and to reflect at the panel edges. These high-frequency fluctuations result in a pronounced acoustic radiation pattern above the vibrating plate, shown in Fig. 5b in terms of the instantaneous pressure field. Downstream of the flexible surface, a regular train of vortical disturbances is observed (Fig. 5c) with characteristic wavelength and frequency compatible with those of Tollmien-Schlichting (T-S) instability. The travelling wave flutter appeared to originate from the coupling of the T-S waves with the panel high-mode transverse fluctuations, and this convective instability ceases below a critical value of Reynolds number.

5. Acknowledgments

The work presented here was sponsored by the U. S. Air Force Office of Scientific Research under Task 2304N402 and was monitored by W. Hilbun and T. Beutner.

References

1. S.K. Lele. Compact Finite Difference Schemes with Spectral-like Resolution. *Journal of Computational Physics*, 103:16-42, 1992.
2. M.R. Visbal and D.V. Gaitonde. High-Order Accurate Methods for Complex Unsteady Subsonic Flows. *AIAA Journal*, 37(10):1231-1239, 1999.
3. D.V. Gaitonde and M.R. Visbal. Further Development of a Navier-Stokes Solution Procedure Based on Higher-Order Formulas. *AIAA Paper 99-0557*, January 1999.
4. D.V. Gaitonde, J.S. Shang, and J.L. Young. Practical Aspects of Higher-Order Numerical Schemes for Wave Propagation Phenomena. *Int. Jnl. for Num. Methods in Eng.*, 45:1849-1869, 1999.
5. D.V. Gaitonde and M.R. Visbal. High-Order Schemes for Navier-Stokes Equations: Algorithm and Implementation into FDL3DI. Technical Report AFRL-VA-WP-TR-1998-3060, Air Force Research Laboratory, Wright-Patterson AFB, 1998.
6. M.R. Visbal and R.E. Gordnier. A High-Order Flow Solver for Deforming and Moving Meshes. *AIAA Paper 2000-2619*, June 2000.
7. M.R. Visbal and D.V. Gaitonde. Computation of Aeroacoustic Fields on General Geometries using Compact-Differencing and Filtering Schemes. *AIAA Paper 99-3706*, June 1999.
8. M.H. Carpenter, D. Gottlieb, and S. Abarbanel. The Stability of Numerical Boundary Treatments for Compact High-Order Finite-Difference Schemes. *Journal of Computational Physics*, 108:272-295, 1993.
9. M.R. Visbal, D.V. Gaitonde, and S.P. Gogineni. Direct Numerical Simulation of a Forced Transitional Plane Wall Jet. *AIAA Paper 98-2643*, June 1998.
10. D. P. Rizzetta, M. R. Visbal, and G. A. Blaisdell. Application of a High-Order Compact Difference Scheme to Large-Eddy and Direct Numerical Simulation. *AIAA Paper 99-3714*, June 1999.
11. D.P. Rizzetta, M.R. Visbal, and D.V. Gaitonde. Direct Numerical and Large-Eddy

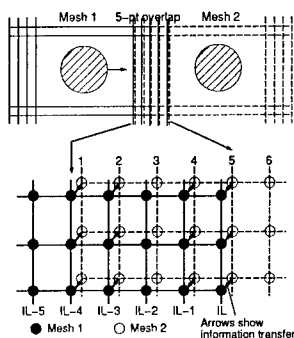


Figure 1. Schematic of mesh overlap for multi-domain strategy

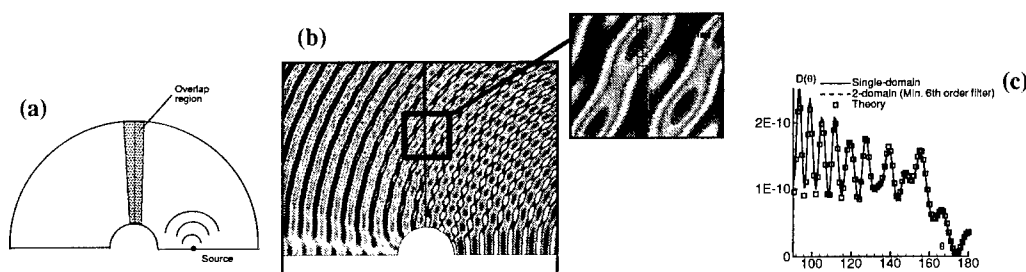


Figure 2. Multi-Domain Acoustic Scattering Simulation

Simulation of Supersonic Flows by a High-Order Method. *AIAA Paper 2000-2408*, 2000.

12. D.V. Gaitonde. Development of a Solver for 3-D Non-ideal Magnetogasdynamics. *AIAA Paper 99-3610*, June 1999.
13. P.D. Thomas and C.K. Lombard. Geometric conservation law and its application to flow computations on moving grids. *AIAA Journal*, 17(10):1030-1037, 1979.
14. R. Beam and R. Warming. An Implicit Factored Scheme for the Compressible Navier-Stokes Equations. *AIAA Journal*, 16(4):393-402, 1978.
15. T.H. Pulliam and D.S. Chaussee. A Diagonal Form of an Implicit Approximate-Factorization Algorithm. *Journal of Computational Physics*, 39(2):347-363, 1981.
16. T. Pulliam. Artificial Dissipation models for the Euler Equations. *AIAA*, 24(12):1931-1940, 1986.
17. D. P. Rizzetta, M. R. Visbal, and M. J. Stanek. Numerical Investigation of Synthetic-Jet Flow Fields. *AIAA Journal*, 37(8), 1999.
18. M.R. Visbal and R.E. Gordnier. Direct Numerical Simulation of the Interaction of a Boundary Layer with a Flexible Panel. *AIAA Paper 2001-2721*, June 2001.
19. M. Visbal and D. Gaitonde. Very high-order spatially implicit schemes for computational acoustics on curvilinear meshes. *J. Comp. Acoustics*, 2001 (In press).
20. M.M. Rai, T.B. Gatski, and G. Erlebacher. Direct simulation of spatially evolving compressible turbulent boundary layer. *AIAA Paper 95-0583*, Jan. 1995.
21. E.T. Spyropoulos. On dynamic subgrid-scale modeling for large-eddy simulation of compressible turbulent flows. *PhD Thesis, Purdue University*, 1996.

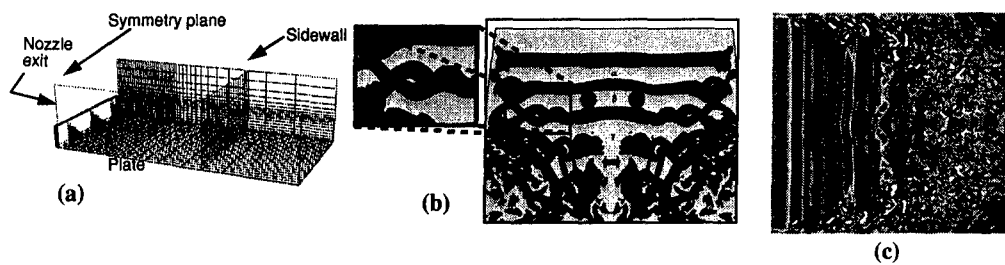


Figure 3. DNS of Forced Transitional Walljet

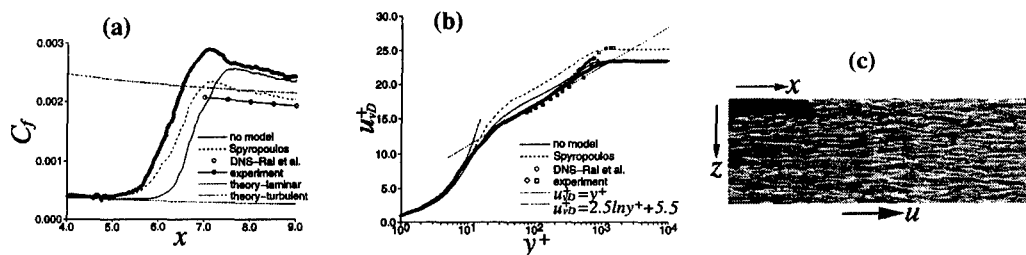


Figure 4. LES of Supersonic Flat-Plate Boundary Layer

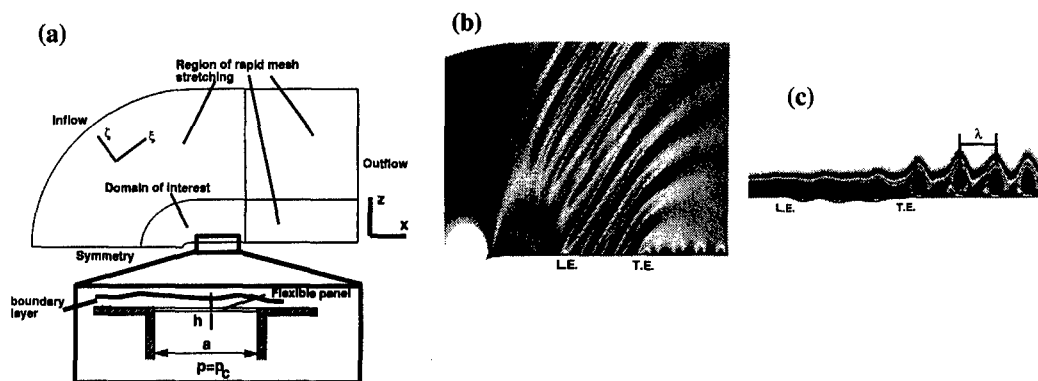


Figure 5. Transitional Boundary-Layer Flow Over a Fluttering Elastic Panel